

Evaporation-driven tear film thinning and breakup in two space dimensions

Qinying Chen¹, Tobin A. Driscoll¹, R. J. Braun¹

¹Department of Mathematical Sciences, University of Delaware, Newark, 19716, DE, USA.

Abstract

Evaporation profiles have a strong effect on tear film thinning and breakup (TBU), a key factor in dry eye disease (DED). In experiments, TBU is typically seen to occur in patterns that locally can be circular (spot), linear (streak), or intermediate. We investigate a two-dimensional (2D) model of localized TBU using a Fourier spectral collocation method to observe how the evaporation distribution affects the resulting dynamics of tear film thickness and osmolarity, among other variables. We find that the dynamics are not simply an addition of individual 1D solutions of independent TBU events, and we show how the TBU quantities of interest vary continuously from spots to streaks for the shape of the evaporation distribution. We also find a significant speedup by using a proper orthogonal decomposition to reduce the dimension of the numerical system. The speedup will be especially useful for future applications of the model to inverse problems, allowing the clinical observation at scale of quantities that are thought to be important to DED but not directly measurable in vivo within TBU locales.

Keywords: Tear film, dry eye disease, lubrication theory, fluorescent imaging, dimension reduction, proper orthogonal decomposition

1 Introduction

Every time one blinks, the upper eyelid drops and then rises to paint a thin liquid film, the tear film (TF), on the eye surface [1]. The healthy TF provides lubrication to the ocular surface and eyelid, antimicrobial defense, a smooth ocular surface for refraction, and a supply of oxygen and nutrition to the avascular corneal epithelium [2, 3]. When the tear film fails, often called tear breakup (TBU), there are adverse stimuli to the ocular surface [4]; chronic TBU and problems with the TF are thought

to be an etiological factor in the development of dry eye disease (DED). DED affects millions of people, with the number depending on the diagnostic criteria used [5]. DED diminishes both quality of vision and ocular surface comfort and health [6]. The major classes of dry eye include evaporative dry eye (EDE) [2]. EDE is thought to be caused by excessive water loss via evaporation [7, 8]. This paper seeks to add to the basic science understanding of evaporative water loss from the TF.

A key mechanism of DED are generally accepted to be tear hyperosmolarity resulting from TF instability [2]. Tear osmolarity is the total concentration of osmotically active solutes, primarily salt ions [9]. Hyperosmolarity is linked to DED [10], but it is not currently possible to measure osmolarity directly in areas of TBU. Osmolarity is measured clinically in the inferior meniscus or outer canthus [11], but these measurements do not reflect the elevated values that may occur over the cornea [12].

The tear film is a thin liquid film with multiple layers that establishes itself rapidly after a blink [13]. The tear film (TF) has three layers: a thin and oily lipid layer that is 20 to 100 nm thick [14], an aqueous layer consisting mainly of water [15] that is a few microns thick, and a half-micron thick mucin layer called the glycocalyx that is on the ocular surface [16]. The lipid layer slows evaporation of water from the TF [17], and a healthy glycocalyx facilitates the fluid movements of the ocular surface [18]. The lacrimal gland supplies the majority of the water from the aqueous layer near the temporal canthus [19]. Osmosis supplies water from the ocular epithelia [20].

TBU happens when a dry spot appears on the eye [21] and is often evaporation-driven [2, 3]. Tear breakup time (TBUT) is the length of time after a blink and before the appearance of the first dry spot [21]. A clinical determination of TBUT is based on the observer's judgment [21] and may incorporate an average of clinicians' estimates [22]. TBUT is a method for determining the stability of the TF and checking for dry eye. A short TBUT is a sign of a poor tear film, and the longer break-up takes, the more stable the tear film [23].

A number of papers have considered a one-dimensional domain that extended across the open eye with fixed ends which typically called post-blink drainage models [24–27]. These models typically imposed large menisci at the domain ends that drained fluid from the relatively flat interior of the TF, and that drove the dynamics. Braun and Fitt [27] included evaporation and found that it could drive thinning to TBU. Heat transfer and evaporation were considered in Li and Braun [28], and later treated together with thermal imaging in Dursch et al. [29].

TBU models are typically along a short line segment and are designed to be local models of TF flow; these models eliminate any influence from the menisci. The effects of evaporation and the Marangoni effect on TBU have been studied in a number of papers. Evaporation drove all the dynamics in the models in [13, 14, 30], though the treatments were different. In [30], a stationary lipid layer (LL) with variable thickness caused increased localized thinning; also included were osmolarity transport in the aqueous layer (AL) and osmosis across the AL/cornea interface. An important result from that work is that diffusion of osmolarity out of the region of evaporation prevents osmosis from stopping thinning as it would in spatially uniform models [14, 20]. Simpler evaporation models were used in [13, 14], but they included transport of fluorescein so that they could explain what was seen in TF visualization experiments. Zhong

et al. [31] developed a PDE model with one spatial variable that incorporated both mechanisms. Including fluorescein dye transport and fluorescence enabled fitting of models to *in vivo* fluorescence data within TBU regions to estimate parameters that are not possible to directly measure there at the time of writing [32, 33]. Recently, ODE models with no space dependence have been successfully fit to fluorescence data in small TBU spots and streaks [34]. Those models have been coupled to a neural-network based data extraction system to greatly expand the amount of TBU instances that may be studied [35]. Other models have provided fundamental analyses on evaporation [36, 37] and instability [38, 39].

Other effects have been included in local models of TBU [13, 30, 31, 40–45]. Some models incorporated the effect of soluble mucins in the AL necessitating departure from more standard lubrication models [43, 44]. Localized non-wettability of the ocular surface was modeled in [45]. Combining this or related theories may be applied to *in vitro* systems of epithelia [46, 47] to shed light on the role of dewetting in TF instability.

Imaging of the tear film is an important tool for analyzing its dynamics. Common imaging techniques include fluorescence (FL) imaging [48], spectral interferometry [49] and optical coherence tomography [50]. Injection of dyes such as fluorescein have been used to stain epithelial cells [21], estimate tear drainage rates or turnover times [51], visualize general TF dynamics [52, 53], estimate TF breakup times [21], and capture the TBU regions. Simultaneous imaging can help interpret TF dynamics [54].

Figure 1 shows the FL images from video captures of three different sustained tear exposure (STARE) trials [55]. As the eye was held open, we observe the emergence and development of small, dark regions. There are mixed patterns for the dark areas: spot-like patterns, which have roughly radial symmetry, streak-like patterns, which are locally one-dimensional, and intermediate shapes. The top right shows a time series of the evolution of a dark spot highlighted in the top left image. The red box in the bottom left image shows a dark spot of indeterminate shape, and the box in the bottom right image shows two connected spots. Our interest is to study these emerging small dark areas from the FL imaging.

Luke et al. [32] developed techniques for fitting experimental data from FL imaging to models given in Braun et al. [13] for evaporation-driven tear film thinning. They found realistic optimal values for peak and baseline evaporation rates and dry spot sizes, and their thinning rate estimates fell within experimental ranges [56]. While the fitting of PDE models in this way [32] was successful, it was slow work, and only twenty instances of TF thinning were fit in that paper. By simplifying the model and automating the TBU instance selection, Driscoll et al. [35] fit hundreds of thinning instances for normal subjects. This approach greatly extended the number of thinning instances that could be analyzed, and the trends remained consistent with PDE models. However, the details of spatial dynamics of thinning and TBU were lost. One clear lesson from these works is that faster computation and fitting of the imaging data could produce much more information about tear film dynamics in human subjects. Another important point is that fitting the models to data could determine important *in vivo* quantities, such as thinning rate, that often require much more complex models to estimate local *in vivo* values (e.g., [29, 30, 57]). Faster simulations to analyze

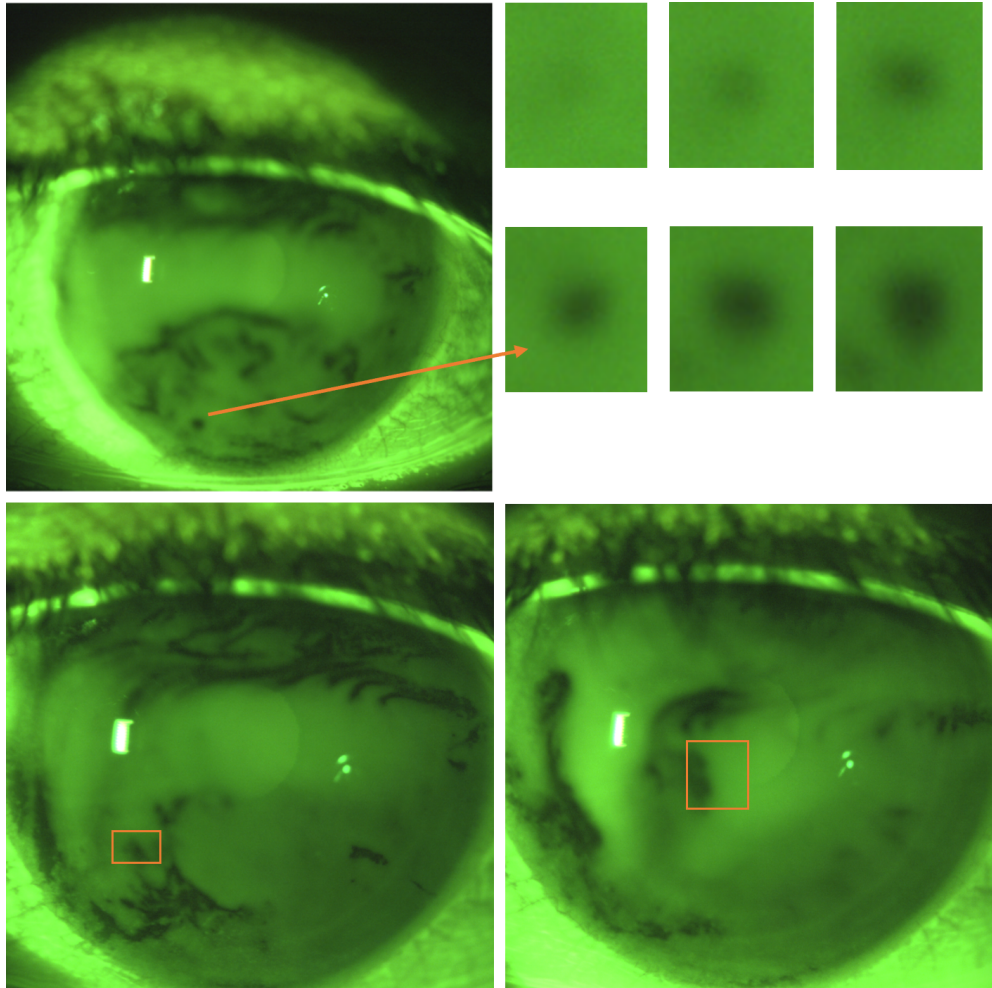


Fig. 1: At top left, bottom left and bottom right are fluorescence images from three different video capture of STARE trials [55]. The top right shows a time series of the evolution of the dark spot highlighted in the top left image. The highlights in the bottom left and bottom right images show respectively an indeterminate shape and a formation of connected spots.(Image courtesy of D.Awisi-Gyau.)

more TBU instances is major motivator for studying the numerical methods applied in this work.

Over the decades, researchers have developed various numerical methods to solve thin film problems. Zhornitskaya & Bertozzi [58] developed positivity-preserving finite difference schemes in one and two space dimensions. Oron & Bankoff [59] used a finite difference scheme based on a spatially uniform staggered grid, and a modified Euler method in time. Schwartz et al. [60] employed a time-marching finite difference method with an alternating-direction-implicit (ADI) technique. Lee et al. [61] used a

full approximation storage (FAS) adaptive multigrid algorithm. Heryudono et al. [62] used a modified Chebyshev spectral collocation for the spatial discretization. Grün & Rumpf [63] presented finite element methods for fourth order degenerate parabolic equations. These methods are all successful for finding a single solution efficiently, but may be slow for repeated solution inside an algorithm.

To our knowledge, Maki et al. [64] were the first to model the human tear film dynamics on a 2D domain. They formulated a relaxation model on an eye-shaped domain with flux boundary conditions, which was solved numerically with a composite overset grid method of 2nd-order finite differences in space together with an adaptive 2nd order BDF time stepping method. The simulation took about two hours on a high-end desktop computer. Li et al. improved the model first by incorporating evaporation and ocular surface wettability [65] and again by incorporating osmolarity transport and osmosis on the 2D eye-shaped domain [66]. The spatial derivatives were discretized using 2nd order finite difference composite overset grids in space as in [64], together with a hybrid time-stepping method, with Runge-Kutta-Chebyshev (RKC) for solving the osmolarity transport and an adaptive BDF method for updating thickness and pressure. The simulation took about 1 to 2 hours on a high-end desktop computer. These 2D simulations are computationally expensive if one wants to do repeated simulations to investigate the effects of the many important parameters or solve inverse problems to fit collected data. proper orthogonal decomposition (POD) method to reduce the computation time as much as possible.

In this paper, we extend the simulation of evaporative models of TBU dynamics to two dimensions (2D) for what we believe to be the first time. As a first step, we simplify the situation to a local model of TF thinning and TBU, as has been done in lower dimensions [13, 14, 30, 32]. Ignoring boundary (e.g., eyelid) effects allows us to employ a Fourier spectral method that can finish accurate simulations in tens of minutes. We further show that the proper orthogonal decomposition (POD) method [67, 68] can reduce the dimensionality of the discretized equations at the cost of a tolerable amount of error, thus greatly accelerating the simulations. Such accelerations will be valuable not only in manually exploring the dynamics within the model but also for solving the inverse problem in future fits to experimental data in the manner of Driscoll et al. [35]. As a step toward understanding TBU dynamics for human ocular surface health, we demonstrate the use of our solution method on exploratory scenarios, such as the transition from (radially symmetric) spot to (mirror-symmetric) streak, the breakdown of radial symmetry, and the merging of nearby dark spots, that provide initial insights into 2D TBU dynamics.

The paper is organized as follows. We present the mathematical model in [section 2](#) in nondimensional form. We present the numerical method, including the use of the POD, in [section 3](#). In [section 4](#) we present simulation results for a variety of scenarios, including replication of the previous results for spots and streaks, and give evidence for the effectiveness of the POD. Finally, in [section 5](#) we discuss the results and describe the next steps for future work.

2 Model

Our model is a two-dimensional version of the models derived by Braun et al. [13] and used by Luke et al. [32] for local TBU dynamics. Li et al [12] derived the 2D model equations in detail, though they were not applied to local TBU dynamics.

The TF is modeled as a Newtonian fluid over a flat corneal surface at the plane $z = 0$. The flat cornea approximation has been justified elsewhere [69, 70], and a 1D model using a curved cornea showed little difference in TF dynamics save for small differences near the lids [71]. Because the film is thin, there is a separation of scales, and lubrication theory may be applied [72, 73].

The key variables in the system are shown in Table 1. These quantities are nondimensionalized according to

$$\begin{aligned} x' &= \ell x, & y' &= \ell y, & z' &= dz, & t' &= \frac{d}{v_{\max}} t, & h' &= dh, & u' &= \frac{v_{\max}}{\epsilon} u. \\ v' &= \frac{v_{\max}}{\epsilon} v, & w' &= v_{\max} w, & J' &= \rho v_{\max} J, & c' &= c_0 c, & f' &= f_{\text{cr}} f, \end{aligned}$$

where primes denote dimensional quantities and the relevant physical parameters are given in Table 2. Other needed nondimensional parameters are given in Table 3.

The derivation of the system follows a typical pattern of deriving thin film models [72, 73]. Scaling produces many factors of $\epsilon = d/\ell \ll 1$ preceding terms that are neglected at leading order. One finds easily that the pressure p is independent of depth and is set by capillarity via the normal stress condition so that it is given by to the curvature of the film surface:

$$p = -\partial_x^2 h - \partial_y^2 h. \quad (1)$$

Integrating mass conservation for the incompressible case (the divergence-free condition) over $0 < z < h(x, y, t)$ and using the boundary conditions results in the mass conservation equation for the film thickness h :

$$\partial_t h + \partial_x(h\bar{u}) + \partial_y(h\bar{v}) = -J + P_c(c - 1) \quad (2)$$

Here \bar{u} and \bar{v} are depth-averaged velocity components along the film in the x and y directions, respectively, arising from solving an approximation of the momentum conservation equation in each direction:

$$\bar{u} = -\frac{h^2}{12} \partial_x p, \quad (3)$$

$$\bar{v} = -\frac{h^2}{12} \partial_y p. \quad (4)$$

The terms involving \bar{u} and \bar{v} determine the change in thickness due to motion of fluid inside the film. J is the thinning rate of the film due to evaporation (discussed below), which appears in the kinematic condition at the air/film interface [20, 72]. $P_c(c - 1)$ is the osmotic supply of water specified by the boundary condition on the transverse velocity component at the film/cornea interface, which approximates the film/cornea

| Variable | Meaning |
|--------------------------|-------------------------------|
| x, y | transverse spatial dimensions |
| z | depth dimension |
| t | time |
| $h(x, y, t)$ | TF thickness |
| $u(x, y, t), v(x, y, t)$ | transverse fluid velocities |
| $p(x, y, t)$ | pressure |
| $J(x, y)$ | evaporation rate |
| $c(x, y, t)$ | osmolarity |
| $f(x, y, t)$ | fluorescein concentration |

Table 1: Variables in the two-dimensional model.

interface as a semipermeable membrane that allows only water to cross [20]. This condition represents the supply of fluid from the cornea as the osmolarity in the film rises as a response to evaporation of water from the film.

Following the approach of Jensen and Grotberg [74] for solutes inside the film (and used in e.g., [13, 20]) one obtains transport equations for the osmolarity c and the FL concentration f . In the resulting equation for the osmolarity, we can interpret certain collections of terms as being responsible for particular mechanisms:

$$\partial_t c + \underbrace{\bar{u}\partial_x c + \bar{v}\partial_y c}_{\text{advection}} = \underbrace{\frac{\partial_x(h\partial_x c) + \partial_y(h\partial_y c)}{h\text{Pe}_c}}_{\text{diffusion}} + \underbrace{\frac{Jc}{h}}_{\text{evap.}} - \underbrace{\frac{P_c(c-1)c}{h}}_{\text{osmosis}}. \quad (5)$$

The transport equation for f is very similar. The evaporation term increases solute concentrations, while osmosis lowers solute concentrations (when osmolarity rises)[12].

The resulting nondimensional system to be solved for the dependent variables h , p , c , and f is

$$\partial_t h + \partial_x(h\bar{u}) + \partial_y(h\bar{v}) = -J + P_c(c-1), \quad (6)$$

$$p = -\partial_x^2 h - \partial_y^2 h, \quad (7)$$

$$h(\partial_t c + \bar{u}\partial_x c + \bar{v}\partial_y c) = \text{Pe}_c^{-1}(\partial_x(h\partial_x c) + \partial_y(h\partial_y c)) + Jc - P_c(c-1)c, \quad (8)$$

$$h(\partial_t f + \bar{u}\partial_x f + \bar{v}\partial_y f) = \text{Pe}_f^{-1}(\partial_x(h\partial_x f) + \partial_y(h\partial_y f)) + Jf - P_c(c-1)f, \quad (9)$$

with parameters given in Table 3. The quantities \bar{u} and \bar{v} are determined by (3) and (4), but they are not dependent variables per se. Note that f appears only in (9), so that equation can be solved separately once the other dependent variables are known.

We apply the equations over a small area of the cornea that is not close to the eyelids and limbus. Because we are not interested in the effects of these boundaries, we assume periodic conditions on all the dependent variables. We also assume that the simulation begins after the eye opens (e.g., as in Figure 6 of [80]) and that all the dependent variables are initially uniform:

$$h(x, y, 0) = c(x, y, 0) = 1, \quad f(x, y, 0) = f_0, \quad (10)$$

| Parameter | Description | Value | Reference |
|--------------|----------------------------------|--------------------------------------------------------|--------------------------|
| μ | Viscosity | 1.3×10^{-3} Pa sec | Tiffany [75] |
| σ_0 | Surface tension | 0.045 N m ⁻¹ | Nagyová and Tiffany [76] |
| ρ | Density | 10^3 kg m ⁻³ | Water |
| d | Initial TF thickness | 4.5 μ m | Calculated |
| ℓ | $(\sigma_0/\mu/v_{\max})^{1/4}d$ | 0.54 mm | Calculated |
| v_{\max} | Peak thinning rate | 10 μ m min ⁻¹ | Nichols et al. [56] |
| V_w | Molar volume of water | 1.8×10^{-5} m ³ mol ⁻¹ | Water |
| D_f | Diffusivity of fluorescein | 0.39×10^{-9} m ² /sec | Casalini et al. [77] |
| D_o | Diffusivity of salt | 1.6×10^{-9} m ² /sec | Riquelme et al. [78] |
| c_0 | Isotonic osmolarity | 300 Osm m ⁻³ | Lemp et al. [11] |
| P_0 | Permeability of cornea | 12.1 μ m/sec | Braun et al. [14] |
| ϵ_f | Napierian extinction coefficient | 1.75×10^7 L m ⁻¹ mol ⁻¹ | Mota et al. [79] |
| f_{cr} | Critical FL concentration | 0.2% | Webber and Jones [51] |

Table 2: Physical parameters (dimensional) used in the governing equations.

| Parameter | Expression | Value |
|------------|--------------------------------------|-----------------------|
| ϵ | d/ℓ | 8.3×10^{-3} |
| α | $(\alpha_0\mu)/(\rho\ell\epsilon^3)$ | 4.06×10^{-2} |
| P_c | $(P_0V_w c_0)/(v_{\max})$ | 0.392 |
| Pe_f | $(v_{\max}\ell)/(\epsilon D_f)$ | 27.7 |
| Pe_c | $(v_{\max}\ell)/(\epsilon D_o)$ | 6.76 |
| ϕ | $\epsilon_f f_{cr} d$ | 0.417 |

Table 3: Typical values of nondimensional parameters that appear in the model (6)–(9) using the parameters in Table 2.

where f_0 is the FL concentration normalized to the critical concentration f_{cr} . For the numerical DAE solver, it is also helpful to supply the initial pressure $p(x, y, 0) = 0$.

The evaporation rate J is our primary input to the model, and it drives all the dynamics. Inhomogeneities in an in vivo lipid layer, sitting atop the aqueous layer of the tear film, are presumed to cause local increases in the evaporation rate, leading to local decreases in h and corresponding increases in the solute concentrations. An example of this sequence occurring in vivo is shown in Figure 6 of King-Smith et al. [80], and simplified models using this idea have appeared, e.g. [13, 14, 30]. We represent the spatial variation of J as one or more localized peaks:

$$J(x, y) = v_b + \sum_{k=1}^K (a_k - v_b) G\left(\frac{x - x_k}{x_{w,k}}, \frac{y - y_k}{y_{w,k}}\right), \quad (11)$$

where $v_b = v_{\min}/v_{\max}$ is a baseline value, (x_k, y_k) is the center of the k th peak, $a_k > v_b$ is the height of the k th peak, $x_{w,k}$ and $y_{w,k}$ are characteristic widths of peak k , and G is the Gaussian

$$G(x, y) = \exp[-(x^2 + y^2)/2]. \quad (12)$$

We note that there was little difference between the resulting images whether one used an evaporation distribution with a very smooth Gaussian or with a sharp-edged

evaporation distribution using a hyperbolic tangent function [13]. We choose to use the smooth Gaussian distribution in this work. Our chosen peak and background values for evaporation are well within experimental observations [56].

The FL intensity I is obtained via [51, 81]

$$I = I_0 \frac{1 - \exp(-\phi fh)}{1 + f^2}, \quad (13)$$

where I_0 is a normalization coefficient and ϕ is the nondimensional Napierian extinction coefficient in Table 3.

Given an evaporation function $J(x, y)$, we solve the system (6)–(9) to obtain h , p , c , and f as functions of space and time. These can then be inserted into (13) to find fluorescent intensity. Note that while equation (9) describes how the evolution of FL concentration f depends on h , p , and c , those quantities do not in turn depend on f . Hence in practice we first solve for the dynamics of h , p , and c , and then use those in a separate stage to solve for f . Once h and f are known, we compute the FL intensity via (13).

3 Numerical methods

For the dynamics we use the method of lines with a Fourier spectral collocation method [82] in space on a uniform periodic grid on the domain $(\pi, \pi)^2$. The number of grid points m and n in each dimension is chosen to be even. The resulting discretization of spatial terms in (6)–(9) creates a differential–algebraic system (DAE) for that is solved in Julia using the QNDF solver, an adaptive quasi-constant time step stiff method in the **DifferentialEquations** package [83] similar to backward differentiation formulas and using Shampine’s accuracy-optimal kappa values as defaults [84]. In cases where the evaporation function J has a single peak centered at the origin, we exploit symmetry by solving only over the first quadrant $[0, \pi]^2$.

The full DAE system has size $\approx 4mn$, with a factor of 4 reduction if symmetry is used. A simulation such as those in section 4 takes several minutes on a typical workstation. In the future, we want to use the DAE solution as the forward method in an inverse solver for potentially hundreds of experimental trials. Thus, acceleration of the forward solver is desirable.

We can greatly reduce the dimension of the discretization via the proper orthogonal decomposition (POD) method [67, 68]. The full-size discrete system may be written generically as

$$\partial_t h(t) = F_h(t, h, p, c), \quad (14a)$$

$$0 = F_p(t, h, p, c), \quad (14b)$$

$$\partial_t c(t) = F_c(t, h, p, c), \quad (14c)$$

where we now use h , p , and c , to denote discretizations of length mn . Suppose that we find the solution over a short time interval $t = (0, \tau)$. Choosing times $t_1 = 0 <$

$t_2 < \dots < t_N = \tau$, we can form the $mn \times N$ matrix

$$H = [h(t_1) \ h(t_2) \ \dots \ h(t_N)]. \quad (15)$$

The POD exploits the fact that the matrix H is often well-represented by a low-rank projection via the SVD. Intuitively, the structure of $h(x, y, t)$ tends to stay close to a manifold of dimension far less than mn .

Thus, we let B_h be the first k left singular vectors of H , where $k \ll N$. Now $B_h^T B_h$ is the $k \times k$ identity and $B_h B_h^T$ is an orthogonal projector onto the column space of B_h . Let $\tilde{h} = B_h^T h$. We now have approximate dynamics to replace (14a):

$$\partial_t \tilde{h} \approx F_h(t, B_h \tilde{h}, p, c). \quad (16)$$

The system (16), however, has large dimension mn . It is reasonable to project it down into the B_h basis via

$$\begin{aligned} B_h^T \partial_t h &\approx B_h^T F_h(t, B_h \tilde{h}, p, c), \\ \partial_t \tilde{h} &\approx B_h^T F_h(t, B_h \tilde{h}, p, c). \end{aligned}$$

We can similarly repeat the projection process for p and c , finding bases B_p and B_c and replacing (14) with the low-dimensional approximation

$$\partial_t \tilde{h}(t) = B_h^T F_h(t, B_h \tilde{h}, B_p \tilde{p}, B_c \tilde{c}), \quad (17a)$$

$$0 = B_p^T F_p(t, B_h \tilde{h}, B_p \tilde{p}, B_c \tilde{c}), \quad (17b)$$

$$\partial_t \tilde{c}(t) = B_c^T F_c(t, B_h \tilde{h}, B_p \tilde{p}, B_c \tilde{c}), \quad (17c)$$

with subsequent lifting to the original discretization grid occurring via

$$h \approx B_h \tilde{h}, \quad p \approx B_p \tilde{p}, \quad c \approx B_c \tilde{c}. \quad (18)$$

Note that the dimensions of the bases B_h , B_p , and B_c do not need to be identical. The savings for using (17) in place of (14) are in the time integration only; the reduced vectors have to be reconstituted onto the original discretization via (18) and manipulated at that size in order to compute F_h , F_p , and F_c . Even so, the savings for the DAE solver are significant.

The typical use of POD is to solve the full system over a relatively short interval $[0, \tau]$, then project to low dimension to continue the evolution. However, we are able to realize substantial additional gains in cases where the evaporation function (11) comprises only one peak or K well-separated peaks. In these cases we can find the full solution for each individual peak at the much lower cost of 1D radial solutions [32]. The tear film equations are in Appendix A for this case. We can solve (A1)–(A5) for each peak while centered at the origin, then shift the center and interpolate the solution to the Cartesian grid as necessary. In the case of the h component, for example, we use 1D solutions to obtain snapshot matrices H_1, \dots, H_K as in (15), then concatenate

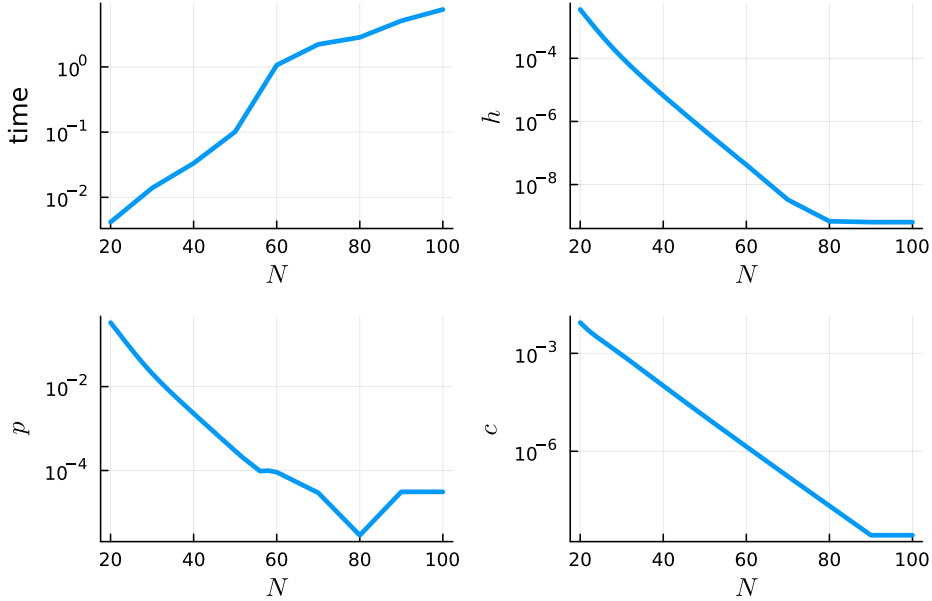


Fig. 2: Top left: Computation time in hours with respect to the Fourier grid resolution N . The other three figures show the relative error at TBUT in the dependent variables h , p , and c .

them horizontally before taking the SVD. This process takes negligible time compared to solving (17), but it produces unsatisfactory approximation bases when the peaks overlap sufficiently, as we show in section 4.

4 Results

We halt simulations when the dimensional thickness of the thinning tear film reaches $1 \mu\text{m}$, since the model is unlikely to be valid as the thickness decreases further. We denote this event as TBU break-up time (TBUT), although we do not claim that it represents a true rupture time in a physically valid model. The results presented in this section were obtained using Julia version 1.8.5 on a Windows laptop with a 12th Gen Intel(R) Core (TM) i7-12700H 2.30GHz processor and 32GB RAM.

Figure 2 shows the computation time and relative error of the solution for increasing grid resolutions. Here we solve (6)–(9) for a single spot centered at origin, with evaporation widths $x_w = y_w = 0.5$, baseline value $v_b = 0.1$, and peak value $a_1 = 1$ in (11). The error is computed at breakup time $t = 2.4$ using a reference solution at grid size $N = 100$ and Fourier interpolation onto matching nodes. We observe that for $N = 60$, the solution is essentially converged in space, suggesting that time-stepping errors become dominant. Since the computation at $N = 100$ takes more than 7 times longer than at $N = 60$, we fix the spatial grid to be 60×60 for all simulations presented in what follows.

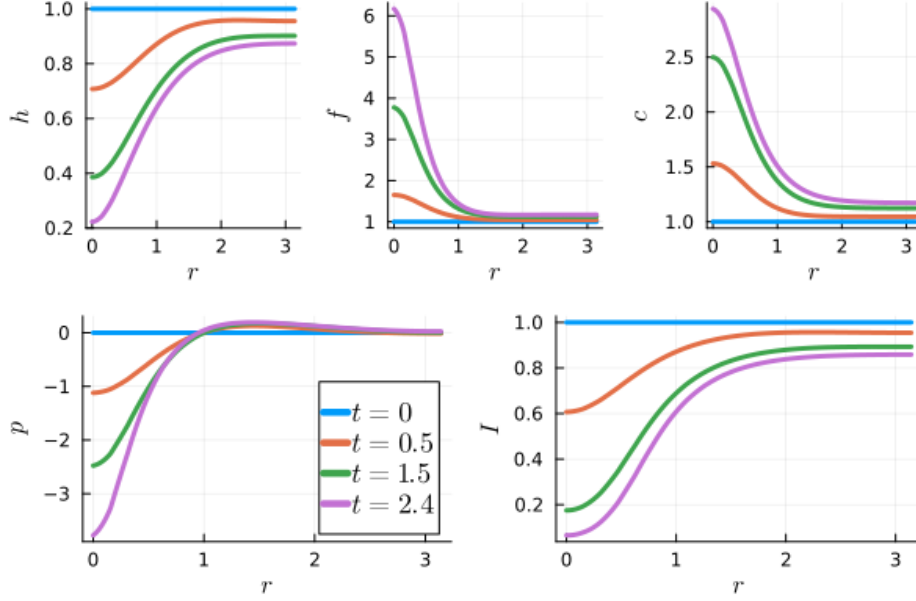


Fig. 3: Nondimensional solution for a single circular evaporation spot, shown as functions of distance r from the center of the spot and time t . The peak evaporation rate is $a_1 = 1$ over a baseline rate of $v_b = 0.1$, and the spot width is $x_w = y_w = 0.5$.

4.1 Single TBU region

We start with $K = 1$ peak in the evaporation function (11). In all the cases of this section, the center of the peak occurs at the origin, i.e., $x_1 = y_1 = 0$.

4.1.1 Circular spot

For the circularly symmetric case with $x_w = y_w$, the problem reduces to the 1D axisymmetric model described in Appendix A and solved previously [13, 32]. This fact allowed us to check the full 2D results against independently generated results from the simpler model that are interpolated onto the 2D grid.

The results for a circular evaporation spot with width $x_w = y_w = 0.5$, peak value $a_1 = 1$, and baseline value $v_b = 0.1$ are shown in Figure 3 as functions of the radius. The integration was halted at TBUT $t \approx 2.4$. We observe that the film is thinnest at the center, which is the same location as the peak evaporation rate. The pressure is lowest at the center and is maximum at around $r = 1$, and the pressure difference, caused by capillarity, drives fluid in towards the middle. The solute concentrations are maximum at the center and increase as time evolves. Finally, FL intensity I is lowest where the thickness h is smallest and FL concentration f is highest.

In order to explore the effects of parameters in the evaporation function J , in Figure 4 we show the intensity and osmolarity function at different time levels for

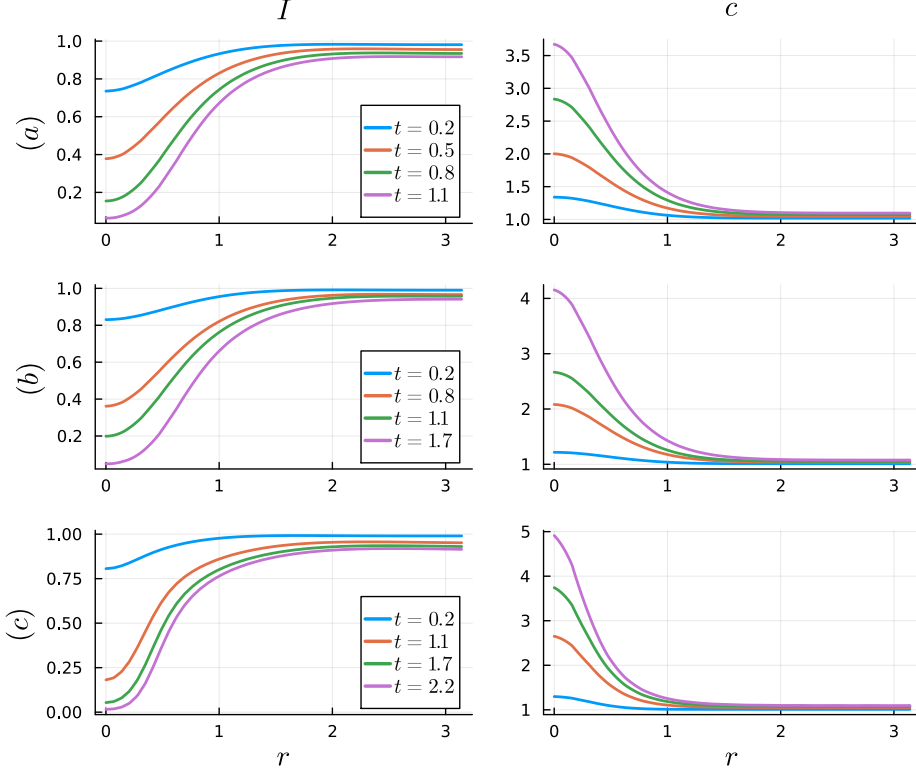


Fig. 4: FL intensity and osmolarity at different time levels for three different one-spot solutions. The TBUTs for cases (a), (b), and (c) in (19) are 1.1, 1.7, and 2.2, respectively.

three different cases over radius r :

$$a_1 = 1.5, \quad v_b = 0.1, \quad x_w = y_w = 0.5, \quad (19a)$$

$$a_1 = 1.0, \quad v_b = 0.05, \quad x_w = y_w = 0.5, \quad (19b)$$

$$a_1 = 1.5, \quad v_b = 0.05, \quad x_w = y_w = 0.3. \quad (19c)$$

The TBUTs for each of these three simulations are 1.1, 1.7, and 2.2, respectively. In case (19a) (first row in the figure), we see a more rapid thinning at the center of the spot due to a larger peak evaporation rate. In case (19b) (second row in the figure), intensity drops quicker, and osmolarity becomes higher over r at the the same time level compared to case (19c) (third row).

Figure 5 shows the central values of dependent variables and the mechanism interpretations given in (5) for diffusion, evaporation and osmosis. We observe that the TBUT is the smallest for case (a); the higher evaporation rate in case (c) is more than

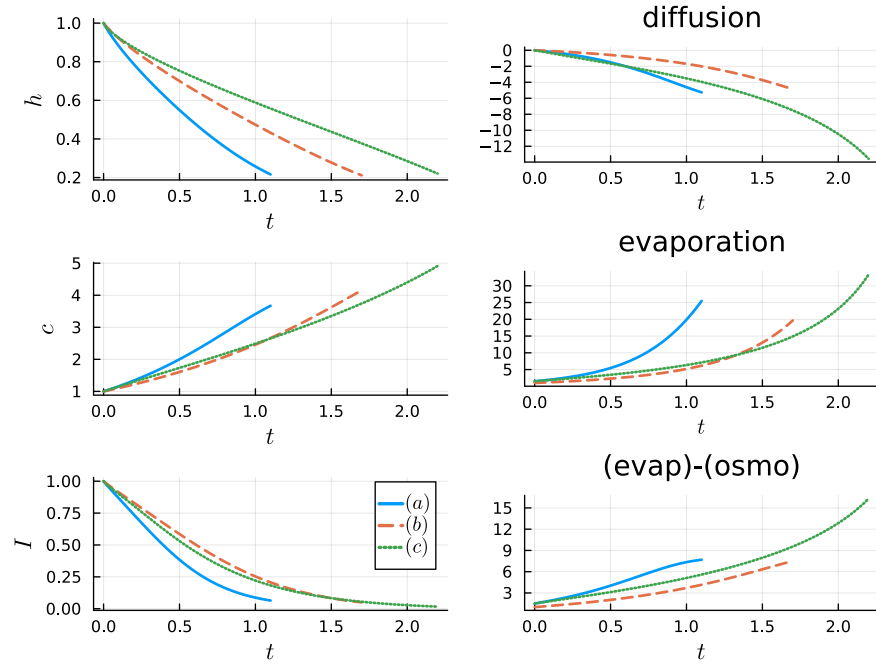


Fig. 5: Left: Central values of tear film thickness, osmolarity and FL intensity for three different spots (19). Right: Dominant terms in the osmolarity equation (5).

counteracted by increased capillary flow. The osmolarity becomes large due to evaporation that is faster than the diffusion. For case (a), around $t = 0.4$, the FL intensity drops to half of its initial values; for cases (b) and (c), the intensity drops to this level at around $t = 0.6$.

4.1.2 Transition from spot to streak

Previous models assumed either axisymmetric spots or streaks with mirror symmetry about a line (e.g., [13, 14, 30–32, 40]), but none, to our knowledge, have studied cases that are intermediate to these. The 2D model allows us to simulate intermediate states that are observed frequently in data [55, 85, 86]. Our 2D periodic boundary conditions do not allow fully 1D streaks, so instead we use different values for $x_{w,1}$ and $y_{w,1}$ in (11) to make ellipses in the level curves of J , and the streak limit corresponds to $x_{w,1} \rightarrow 0$. We use peak evaporation rate $a_1 = 1$ and the baseline rate $v_b = 0.1$ throughout this section. We approach the spot-to-streak transition in two different ways.

Fixed total evaporation rate. In this approach, the product $x_w y_w$ is kept fixed at $\frac{1}{4}$ in order to keep the total evaporation rate constant; i.e., the total amount of water lost, as represented by the double integral of J , is constant for different shapes.

Figure 6 shows the central values of variables as functions of time for $x_w = 0.5$, 0.35, and 0.25 for increasing eccentricity. The TBUT for these cases are $t = 2.4$, 2.65, and 3.4, respectively, showing that the breakup occurs more slowly for streaks than for spots. The axisymmetric spot shows both a higher FL concentration and osmolarity at the center at a fixed time than in the eccentric cases. Figure 7 compares the sizes of the mechanisms labeled in (5), exclusive of advection, which is close to zero here. At a fixed time, the spot TBU has a less diffusion, more evaporation, and more net thinning from the difference between evaporation and osmosis, than the eccentric cases. At TBUT, that is, at the ends of the curves, the ordering of the terms is reversed. Figure 8 shows snapshots of the FL intensity in these three cases. We note that the levels of intensity, once they become dark enough (say $I \leq 0.25$), are difficult to distinguish visually.

In order to more easily compare these three cases, we turn to one-dimensional plots of the results at the end of the computations. Figure 9 shows the values of h , c , f , and I in these cases along the x -axis at their respective TBUTs. The curves for h show only weak influence from the evaporative width, as its length scale is dominated by the surface tension. The effect of diffusion is apparent in the lowering of the peak osmolarity value as the simulation lasts longer for larger TBUT. The FL concentration is more strongly affected by advection than osmolarity, and this is evident from the fact that higher values occur centrally for larger TBUTs. The intensity profiles depend on both h and f , so that results for this variable are intermediate.

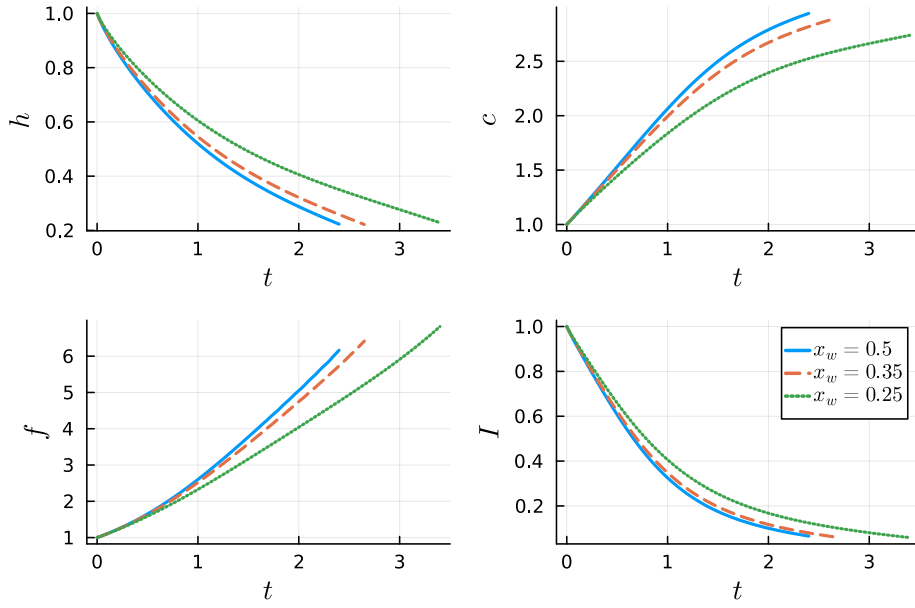


Fig. 6: Central values of h , c , f , and I for spot-to-streak transition with fixed product of peak widths $x_w y_w = \frac{1}{4}$, baseline rate $v_b = 0.1$, and peak evaporation rate $a_1 = 1$. The evaporation width x_w is 0.5, 0.35, 0.25, and the TBUT are 2.4, 2.65, 3.4 respectively.

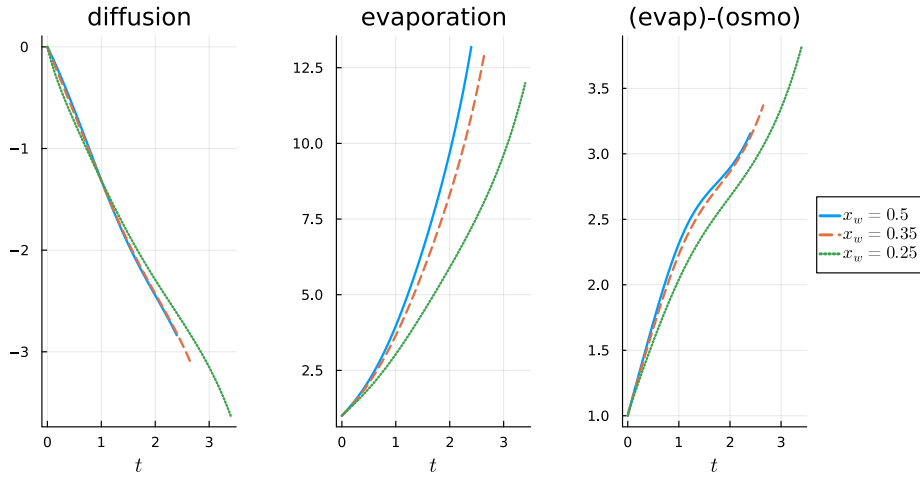


Fig. 7: Dominant terms in the osmolarity equation (5). The parameters for the evaporation function are the same as in the simulations for Figure 6.

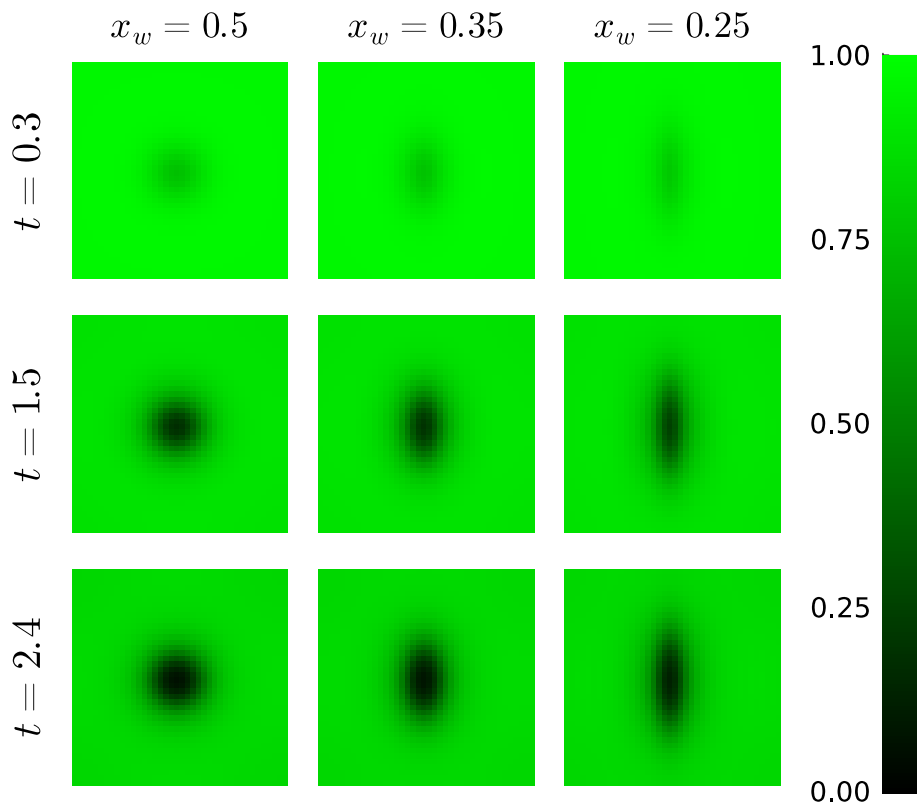


Fig. 8: FL intensity for spot-to-streak transition under the same parameters as in [Figure 6](#) with fixed product $x_w y_w = \frac{1}{4}$.

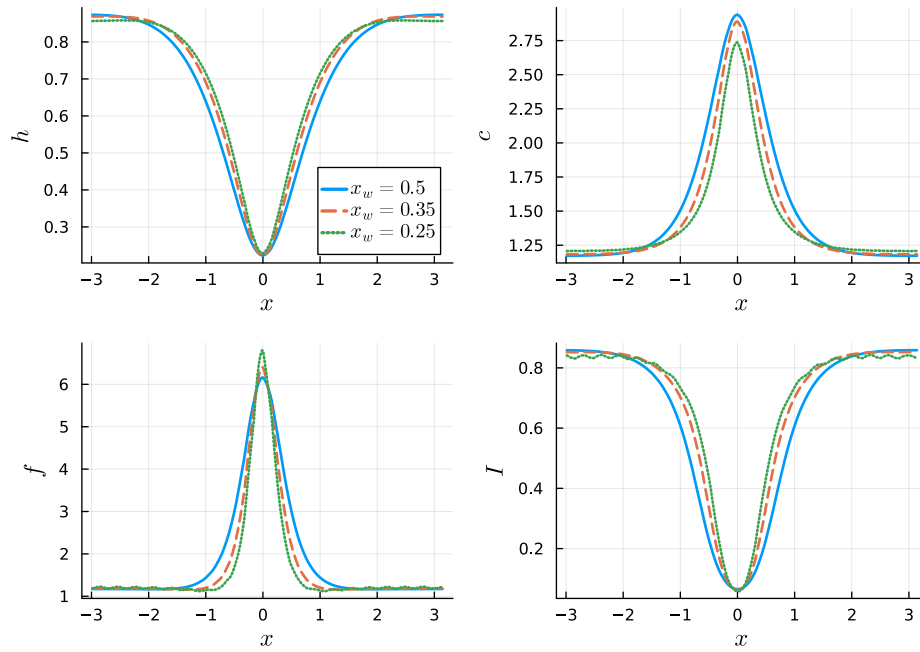


Fig. 9: Values of h , c , f , and I along the x axis at TBU time under the same parameters as in [Figure 6](#).

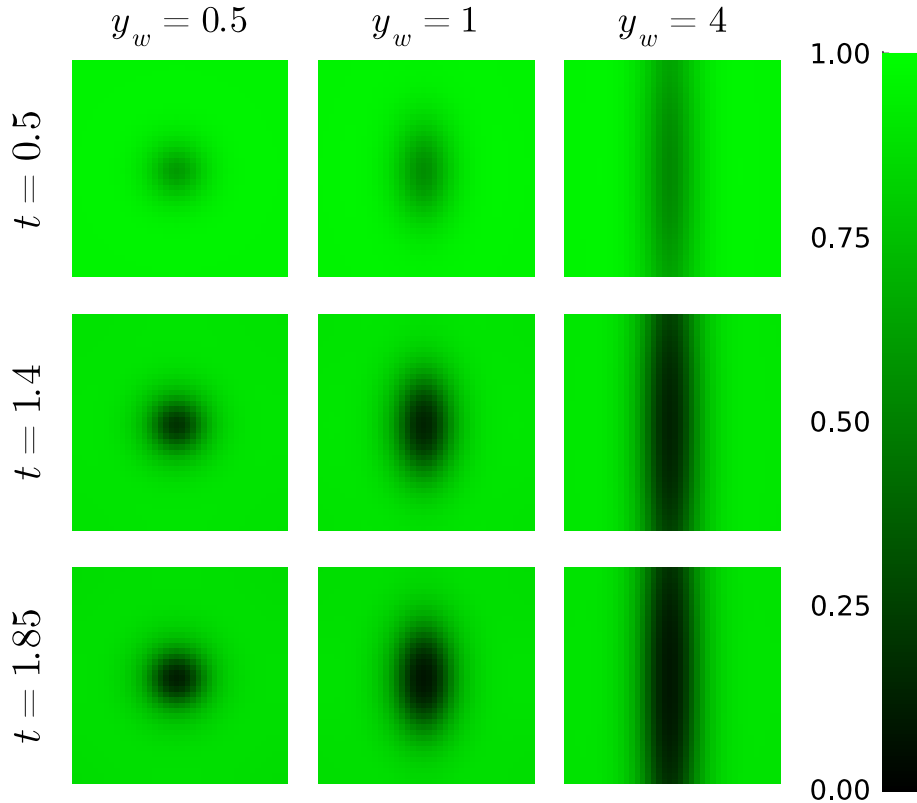


Fig. 10: FL intensity for spot and ellipse TBU with fixed $x_w = 0.5$ at three time levels. From left to right, the evaporation width y_w is 0.5, 1, 4 respectively.

Fixed width in the evaporation function. In this approach, we leave the Gaussian width x_w fixed at $\frac{1}{2}$ while $y_w \rightarrow \infty$, along with $v_{max} = 1$ and $v_b = 0.1$. The second approach may be relevant to tears because the v_{max} and v_b may be roughly constant in a given eye, and so different shapes may allow different amounts of water to evaporate. It also allows us to compare directly with the fully 1D streak limit [13]. Note that in this case, $y_w \rightarrow \infty$ increases the volume of water lost to evaporation for the same time interval compared to fixing the product $x_w y_w$. Figure 10 shows snapshots of the FL intensity for $y_w = 0.5, 1, 4$, in which the TBUT are 2.4, 1.9, 1.85, respectively. We observe that at $y_w = 4$, the solution looks indistinguishable from a streak, which has TBUT 1.87. The left column in Figure 11 shows the central values of key quantities for these cases, along with the 1D streak limit, again showing little difference between $y_w = 4$ and a true streak. We also observe that the streak has the highest osmolarity at TBUT, while the spot has the highest FL concentration at TBUT. The right column shows results for connected spots, which we will discuss in subsection 4.2.

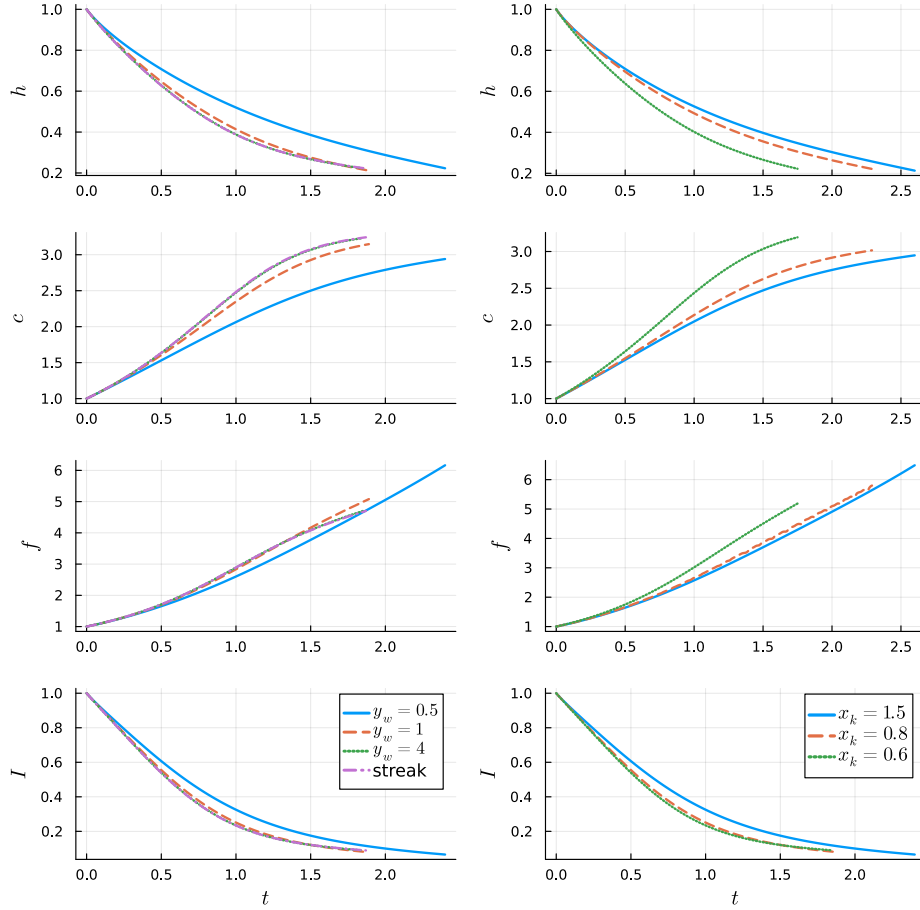


Fig. 11: Left column: Central values of key quantities for TBU with evaporation functions in elliptical patterns of varying eccentricity. Also shown is a 1D streak solution, which is indistinguishable from the most eccentric case. Right column: Central values for circular spots of differing separation half-distances of $x_k = 1.5, 0.8$, and 0.6 ; see [subsection 4.2](#).

[Figure 12](#) shows the dominant terms in the osmolarity equation (5) for the second type of spot-to-streak transition. The spot has a larger diffusion and smaller evaporation compared to the other cases, leading to a lower osmolarity. We also observe that for a streak, the difference between evaporation and osmosis reaches a peak and then decreases as we approach TBU. This is because the larger evaporation results in a higher osmolarity, leading to increased osmotic flow.

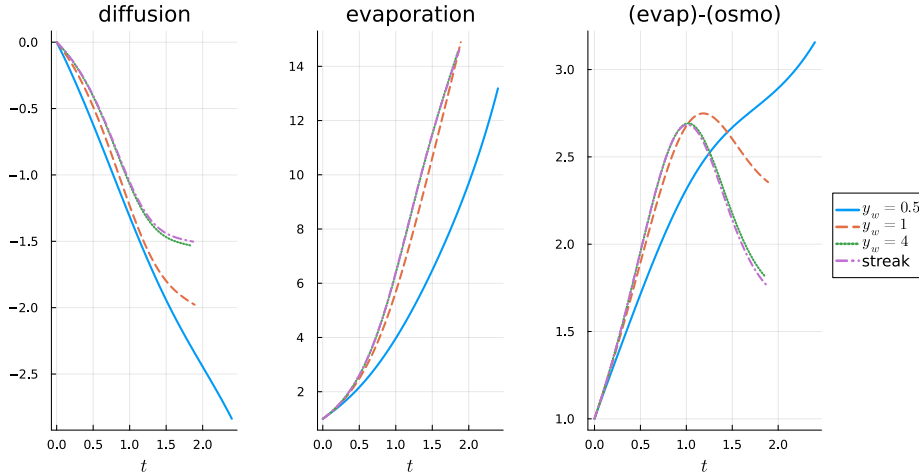


Fig. 12: Dominant terms in the osmolarity equation (5). The parameters for the evaporation function are the same as in the simulations for the left column in Figure 11.

4.1.3 Effectiveness of the POD method for a single spot

In Figure 13 we present the relative error between our POD model and true solution for a single spot centered at the origin with evaporation width $x_w = y_w = 0.5$, peak evaporation rate $a_1 = 1$ and baseline rate $v_b = 0.1$. The result in the plot is obtained by first solving (14) over the time domain $t = [0, \tau]$ to obtain the POD basis as described in section 3, then solving the reduced-dimension system starting again from $t = 0$ to obtain the solution up to TBUT. The resolution for the spatial domain is 60×60 over $[-\pi, \pi] \times [-\pi, \pi]$. We plot for the three cases $\tau = 0.25, 0.5, 1$, and the number N of time steps in the captured snapshots in the solution matrix H in (15) is 40, 50, 100 respectively. Increasing N beyond these values does not improve the solution noticeably. Since the pressure is essentially a second derivative of h , it is the component with the largest error. The numbers of basis vectors for B_h, B_p, B_c for the three cases in the figure are (15, 25, 15), (20, 30, 20), and (40, 50, 40) respectively. We do not show the errors of the f component because they are similar to those for c .

In Figure 13 we see significant improvement in the accuracy when τ is changed from 0.25 to 0.5. But there is much less improvement when τ is increased again to 1. In most cases the error in the solution components begins to increase sharply at some time $t > \tau$, although this sudden change does not appear in the derived I quantity. Based on these observations, and because the runtime is more or less proportional to τ , we use $\tau = 0.5$ in all the simulation results we present. Thus, when the TBUT is around 2, for instance, we have achieved a 4x speedup.

For circularly symmetric evaporation patterns, without going through (14), we take advantage of the 1D radial solver, and we solve on $t = (0, 3)$ since it only takes about two more seconds for 1D solver compared to solving on $t = (0, 0.5)$.

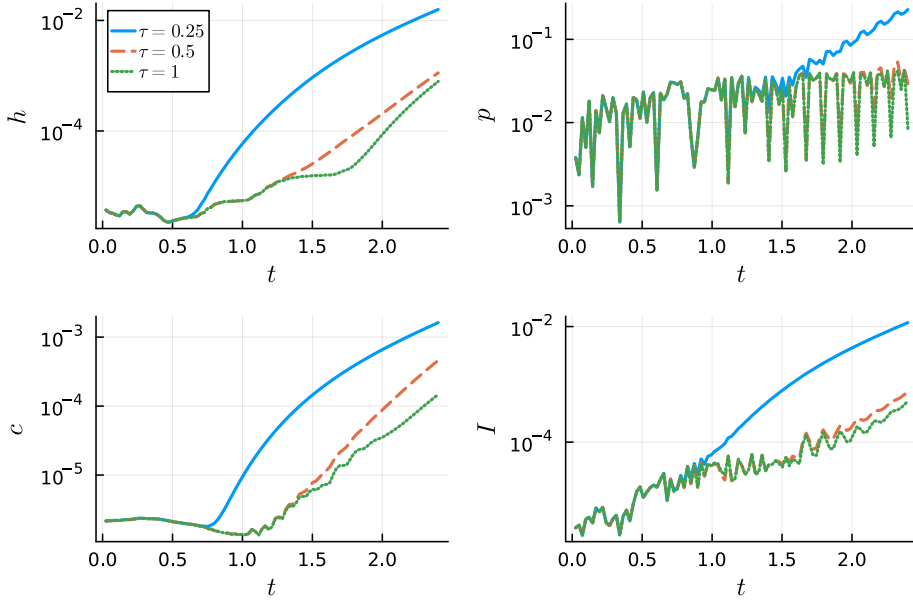


Fig. 13: Relative error of h, p, c, I between POD solution and true solution for a single spot with respect to time. Color indicates different τ values. Log scale is used for the y axis.

On a 50×50 spatial grid, the computation time for a single spot centered at origin using the original Fourier discretization (14) over $t \in [0, 2.4]$ is approximately 2 minutes. The computation time for using (14) on $t = (0, 0.5)$ is about 30 seconds, and then computing the POD basis and solving the reduced system (17) takes about another 30 seconds on $t \in [0, 2.4]$; thus, about half of the total computation time was saved by using the POD. As the discretization dimension increases, however, the cost of solving (14) increases dramatically. On a 60×60 spatial grid, for instance, the full solution takes about 40 minutes, compared to 10 minutes over $t \in [0, 0.5]$ followed by just 35 seconds for the POD method. In other words, the cost of the POD is essentially entirely due to the full solution step for the initial part of the time evolution, and the low-dimensional projection over the rest of the time domain comes for free.

| Figure | Spot 1 | | | Spot 2 | | |
|-----------------------------|--------|--------------|----------------------|--------|--------------|----------------------|
| | a_1 | (x_1, y_1) | $(x_{w,1}, y_{w,1})$ | a_2 | (x_2, y_2) | $(x_{w,2}, y_{w,2})$ |
| Figure 14 (left) | 1 | $(-1.5, 0)$ | $(0.5, 0.5)$ | 1 | $(1.5, 0)$ | $(0.5, 0.5)$ |
| Figure 14 (second to left) | 1 | $(-1.5, 0)$ | $(0.5, 0.5)$ | 0.5 | $(1.5, 0)$ | $(0.5, 0.5)$ |
| Figure 14 (second to right) | 1 | $(-1.5, 0)$ | $(0.5, 0.5)$ | 1 | $(1.5, 0)$ | $(0.2, 0.2)$ |
| Figure 14 (right) | 1 | $(-1.5, 0)$ | $(0.25, 1)$ | 1 | $(1.5, 0)$ | $(0.5, 0.5)$ |

Table 4: Parameters in the evaporation function (11) for the simulations shown in Figure 14. All have $K = 2$ spots and baseline evaporation rate $v_b = 0.1$.

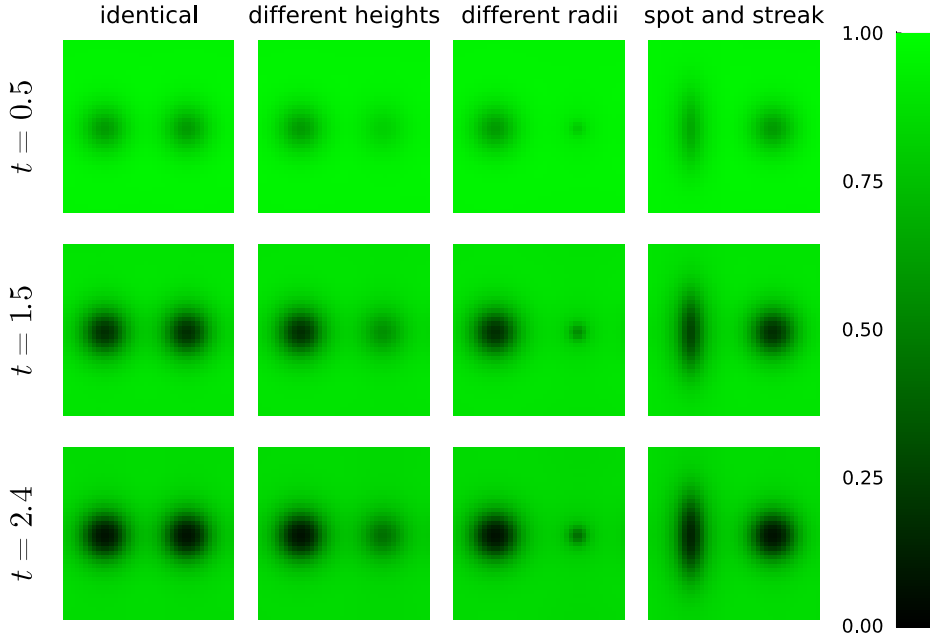


Fig. 14: Snapshots of FL intensity for four cases of two well-separated evaporation regions; the parameters are given in Table 4.

4.2 Multiple TBU regions

Figure 14 shows snapshots of the FL intensity for four different evaporation patterns with multiple thinning regions. The parameters of the evaporation function for these cases are given in Table 4. From left to right, the columns represent: two identical spots; two same-sized spots with different peak evaporation rates; two spots with different radii but the same peak evaporation rates; and one spot and one thin ellipse. The TBUTs for all four simulations are, respectively, 2.6, 2.58, 2.49, and 2.57.

The rest of this section focuses on three cases having evaporation patterns with identical circular spots that are separated by differing amounts. For the evaporation function $J(x, y)$ in (11), we set $a_k = 1$ for both spots, $v_b = 0.1$, and $x_{w,k} = y_{w,k} = 0.5$ in all three cases. We adjust the center positions, located at $\pm x_k$, using the three values $x_k = 1.5, 0.8,$ and 0.6 , respectively, and fix $y_k = 0$. The TBUT for each case is 2.6,

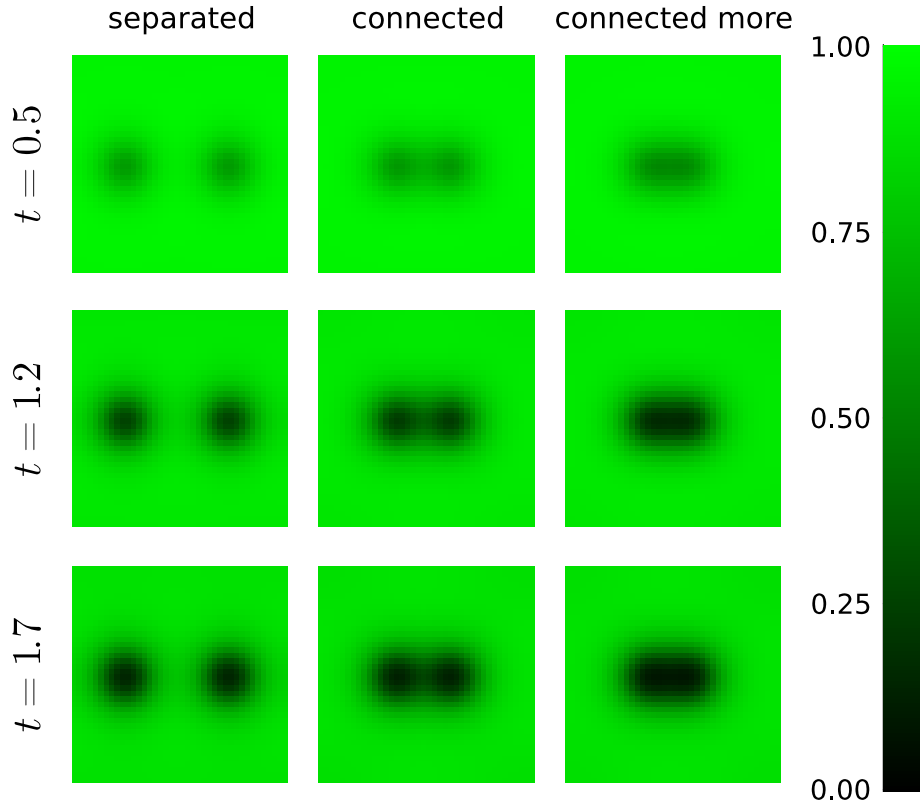


Fig. 15: FL intensity contours at three different time levels for two spots from separated to connected. From left to right: $x_k = 1.5$, 0.8 , and 0.6 .

2.3, and 1.7, respectively, decreasing (as we show below) due to increased evaporative effects.

Figure 15 shows the FL intensity at three time levels for each of these cases, with connectedness between the spots increasing from left to right. Referring back to Figure 11, the right column shows the central values located at $\pm x_k$ of the dependent variables. The central values for the largest separation are very similar to the single-spot case, which is the blue line in the left column of that figure, though they occur slightly later because of the larger TBUT. As the separation decreases, the TBUT decreases as well. The central values for the smaller x_k are distinct from the central values from the elliptical cases in Figure 11. Even though the TBUT is different, we observe that for $x_k = 0.6$, which is the green dashed line in the second column, the osmolarity is very close to that of the streak case, indicating that the connected spots would behave similarly to a single streak or eccentric ellipse.

Figure 16 shows the dominant terms in the osmolarity equation (5). We observe that as the separation distance decreases, the evaporation and diffusion increase,

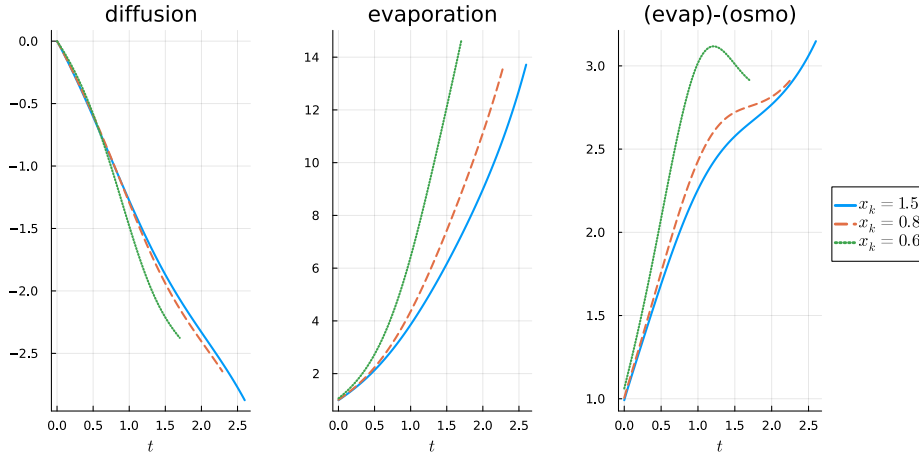


Fig. 16: Dominant terms in the osmolarity equation (5). The parameters for the evaporation function are the same as in the simulation for right column in Figure 11, Figure 17 and Figure 18.

accounting for the faster TBU. For $x_k = 0.6$, the difference between evaporation and osmosis decreases in the end, showing that osmosis is increasing.

Figure 17 shows the dependent variables along the x axis (i.e., the separation axis) at TBUT. These plots are symmetric in x because the spots are identical. The curves in the least-separated case $x_k = 0.6$ suggest that the two spots have nearly fully merged.

Finally, Figure 18 shows in greater detail how the osmolarity at TBUT, and TBUT itself, vary with the separation distance. Up to a separation of $x_k = 0.5$, which is the characteristic spot width $x_{w,k}$, the peak value of osmolarity at the spot centers practically coincides with the value at the origin, while the TBUT roughly doubles from the overlapped case. As the separation distance continues to increase, the peak osmolarity and TBUT level off at about $x_k = 1$, suggesting that the spots no longer meaningfully interact beyond this distance. The asymptotic value of peak osmolarity is about 72% of its full-overlap value, while the asymptotic TBUT is about 3 times the overlap value.

4.2.1 Performance of POD for connected spots

For a single circular spot, we were able to use a 1D radial solver in place of the full 2D solution in order to quickly get numerical basis vectors for the POD method. With two well-separated spots, this technique can still be applied to the spots independently to construct the POD basis, but the error suffers as the separation decreases and the POD basis misses crucial information about the interaction between spots. Figure 19 shows the relative error of the two POD variants for the two connected spots in the third column in Figure 15. The blue solid curve represents the POD solution obtained via 1D radial solver, and the red dashed curve represents the POD solution obtained via the 2D solver. The radial POD solution reaches essentially 100% error well before

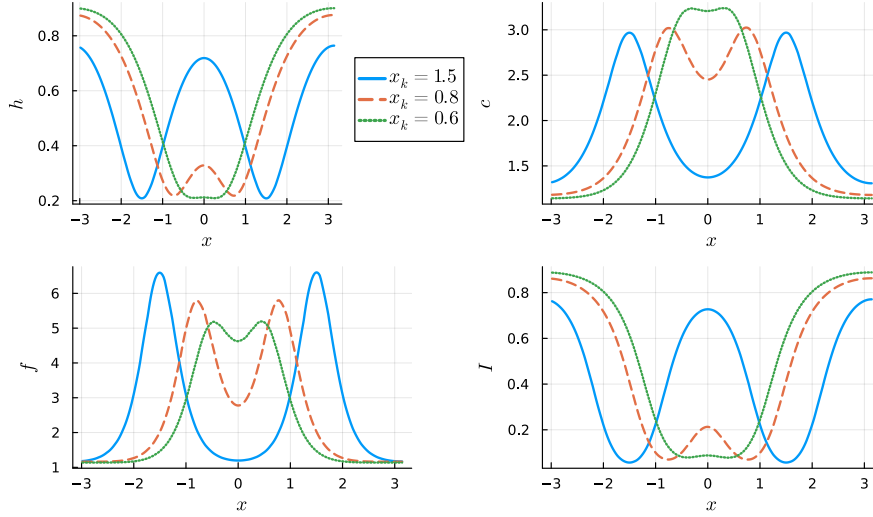


Fig. 17: Values of h, c, f, I along the separation axis at TBUT for identical spots with different separation half-distances x_k .

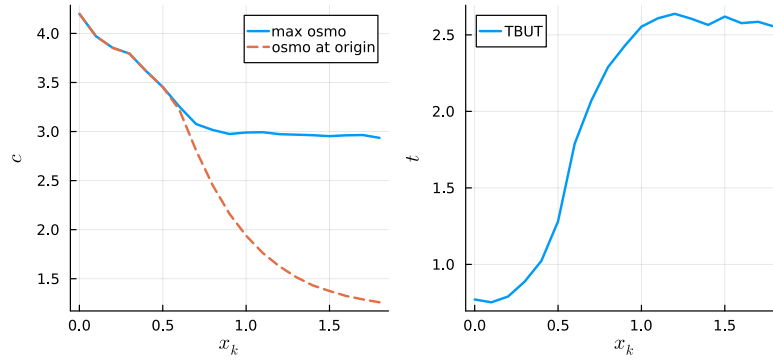


Fig. 18: Left figure: Blue solid line shows the maximum osmolarity for two connected spots with varying x_k ; Red dash line shows the osmolarity at the center of two connected spots. Right figure shows the TBUT with respect to x_k .

TBUT, while the 2D POD stays below 10% error. Although this observation is made purely from the standpoint of the performance of a numerical method, it provides further support for the conclusion that when two spots are close enough together, they behave very differently from two superimposed spots.

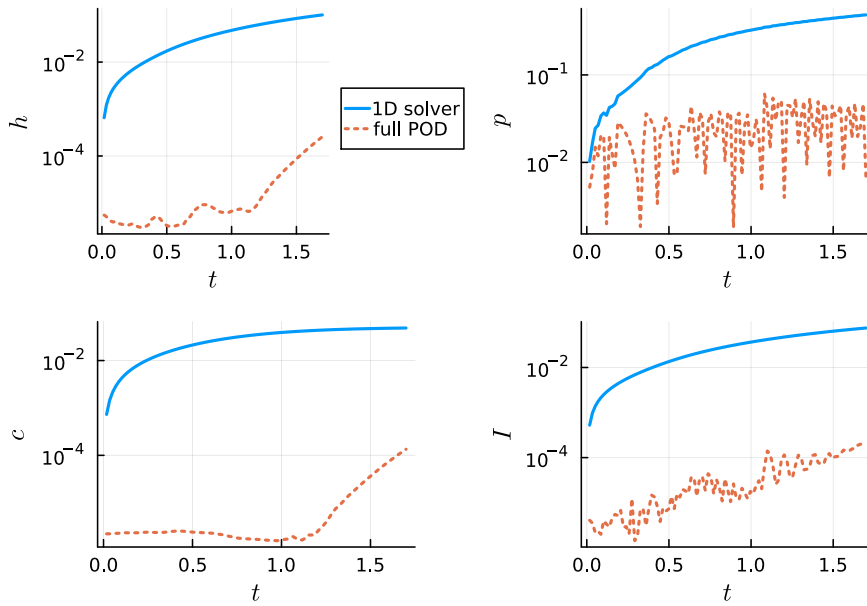


Fig. 19: Relative error for two variants of the POD dimension reduction method for two interacting evaporative spots.

5 Conclusion

In broad terms, there is a good resemblance between the time evolution of fluorescent intensity in our computational results, like those in [Figure 8](#) and [Figure 10](#), and in small patches within the experimental video data like those exhibited in [Figure 1](#). By varying the evaporation rate function, we can reproduce features seen in experiments, such as isolated spots and streaks as well as mixed shapes. We found, for instance, that once the aspect ratio of the ellipses for the evaporation function reaches 2 (i.e., $y_w/x_w = 2$), the TBU dynamics closely approximates a streak. In other words, when we have the relatively small distortion $y_w/x_w = 2$, the central values of the solution from this elliptical distribution of evaporation are already a very good approximation to the solution for a streak ($y_w/x_w \rightarrow \infty$).

While our model does not account for every known effect within the tear film and ignores boundary effects near the eyelids, experience has shown [[32–35](#)] that even limited models can be fit accurately to experimental FL data; in fact, our model can be seen as a direct 2D generalization of the 1D models in [[32](#)]. Given the considerable modeling and computational challenges of complete 2D global behavior of the tear film, first investigating the utility of a restricted model is an attractive approach.

Our next step will be to solve inverse problems for this model to get quantitative agreement with individual experiments, thus producing insights about thinning mechanisms and critical unobservable quantities such as local osmolarity. Since inverse problems necessitate multiple forward solutions and we intend to attempt fitting at many sites within individual trials over potentially hundreds of trials, computational efficiency of the forward solution is a major issue. This motivated our choice of Fourier discretization in space, which is the most efficient way to model smooth solutions in an interior domain.

The inherent stiffness of the resulting DAE problem makes time-stepping difficult, and we have applied the POD method to project the system into far fewer dimensions to accelerate the solution process after a fixed time interval. The computational time for finding the reduced basis and solving the reduced model is insignificant compared to the full model. We have shown speedups of fourfold or more while keeping errors at a tolerable level. Although we have not seen the POD method applied to systems with mass matrices elsewhere, that extension was straightforward, and there does not seem to be anything particular to this system that makes it especially challenging for POD.

Declarations

Funding. This work was supported by National Science Foundation grant 1909846. Any opinions, findings, and conclusions or recommendations expressed in this material are those of the authors and do not necessarily reflect the views of the National Science Foundation.

Conflict of Interest. The authors declare no competing interests.

Appendix A Axisymmetric model

For the circular case, we use the axisymmetric coordinates (r', z') to denote the position and $u' = (u', w')$ to denote the fluid velocity. The tear film is modeled as an incompressible Newtonian fluid on $0 < r' < R_0$ and $0 < z' < h'(r', t')$. The scalings and non dimensional parameters are similar in [Table 2](#) and [Table 3](#). The only difference is that $r' = \ell r$. Braun et al. derived the system of equations on the domain $0 < r < R_0$ [[13](#), [14](#)].

$$\partial_t h + \partial_r(rh\bar{u}) = -J + P_c(c - 1), \quad (\text{A1})$$

$$\bar{u} = -\frac{h^2}{12}\partial_r p, \quad (\text{A2})$$

$$p = -\frac{1}{r}\partial_r(r\partial_r h), \quad (\text{A3})$$

$$h(\partial_t c + \bar{u}\partial_r c) = \text{Pe}_c^{-1}\frac{1}{r}\partial_r(rh\partial_r c) + Jc - P_c(c - 1)c, \quad (\text{A4})$$

$$h(\partial_t f + \bar{u}\partial_r f) = \text{Pe}_f^{-1}\frac{1}{r}\partial_r(rh\partial_r f) + Jf - P_c(c - 1)f, \quad (\text{A5})$$

The evaporation function J is

$$J(r) = v_b + (a - v_b) \exp[-(r/r_w)^2/2]. \quad (\text{A6})$$

where v_b is the ratio of v_{\max} over v_{\min} , r_w is the radius, and $a > v_b$ is the height of the peak.

Appendix B Full streak model

The linear case model is solved on the Cartesian coordinates $-\pi < x < \pi$ and $0 < z < h(x, t)$. More details about derivation can be found in [[13](#), [14](#)]. Periodic boundary conditions are applied.

$$\partial_t h + \partial_x(h\bar{u}) = -J + P_c(c - 1), \quad (\text{B7})$$

$$\bar{u} = -\frac{h^2}{12}\partial_x p, \quad (\text{B8})$$

$$p = -\partial_x^2 h, \quad (\text{B9})$$

$$h(\partial_t c + \bar{u}\partial_x c) = \text{Pe}_c^{-1}\partial_x(h\partial_x c) + Jc - P_c(c - 1)c, \quad (\text{B10})$$

$$h(\partial_t f + \bar{u}\partial_x f) = \text{Pe}_f^{-1}\partial_x(h\partial_x f) + Jf - P_c(c - 1)f, \quad (\text{B11})$$

The evaporation function J is

$$J(x) = v_b + (a - v_b) \exp[-(x/x_w)^2/2]. \quad (\text{B12})$$

The parameters are identical as in the spot case, and r, r_w simply been replaced by x, x_w here.

References

- [1] Doane, M.G.: Interaction of eyelids and tears in corneal wetting and the dynamics of the normal human eyeblink. *Am. J. Ophthalmol.* **89**, 507–516 (1980)
- [2] Lemp, M.A.: The definition and classification of dry eye disease: Report of the Definition and Classification Subcommittee of the International Dry Eye WorkShop (2007). *Ocul. Surf.* **5**(2), 75–92 (2007)
- [3] Willcox, M.D.P., Argüeso, P., Georgiev, G.A., Holopainen, J.M., Laurie, G.W., Millar, T.J., Papas, E.B., Rolland, J.P., Schmidt, T.A., Stahl, U., Suarez, T., Subbaraman, L.N., Uçakhan, O.Ö., Jones, L.: TFOS DEWS II Tear Film Report. *Ocul. Surf.* **15**(3), 366–403 (2017)
- [4] King-Smith, P.E., Begley, C.G., Braun, R.J.: Mechanisms, imaging and structure of tear film breakup. *The ocular surface* **16**(1), 4–30 (2018)
- [5] Stapleton, F., Alves, M., Bunya, V.Y., Jalbert, I., Lekhanont, K., Malet, F., Na, K.-S., Schaumberg, D., Uchino, M., Vehof, J., Viso, E., Vitale, S., Jones, L.: TFOS DEWS-II epidemiology report. *Ocul. Surf.* **15**(3), 334–365 (2017)
- [6] Nelson, J.D., Craig, J.P., Akpek, E.K., Azar, D.T., Belmonte, C., Bron, A.J., Clayton, J.A., Dogru, M., Dua, H.S., Foulks, G.N., Gomes, J.A.P., Hammitt, K.M., Holopainen, J., Jones, L., Joo, C.-K., Liu, Z., Nichols, J.J., Nichols, K.K., Novack, G.D., Sangwan, V., Stapleton, F., Tomlinson, A., Tsubota, K., Willcox, M.D.P., Wolffsohn, J.S., Sullivan, D.A.: TFOS DEWS II Introduction. *Ocul. Surf.* **15**(3), 269–275 (2017)
- [7] Lin, H., Yiu, S.C.: Dry eye disease: A review of diagnostic approaches and treatments. *Saudi J. Ophthalmol.* **28**(3), 173–181 (2014)
- [8] Baudouin, C., Aragona, P., Messmer, E.M., Tomlinson, A., Calonge, M., Boboridis, K.G., Akova, Y.A., Geerling, G., Labetoulle, M., Rolando, M.: Role of hyperosmolarity in the pathogenesis and management of dry eye disease: Proceedings of the OCEAN group meeting. *Ocul. Surf.* **11**, 246–258 (2013)
- [9] Stahl, U., Willcox, M., Stapleton, F.: Osmolality and tear film dynamics. *Clin. Exp. Optom.* **95**(1), 3–11 (2012)
- [10] Tomlinson, A., Khanal, S., Ramaesh, K., Diaper, C., McFadyen, A.: Tear film osmolarity: Determination of a referent for dry eye diagnosis. *Invest. Ophthalmol. Vis. Sci.* **47**(10), 4309–4315 (2006)
- [11] Lemp, M.A., Bron, A.J., Baudouin, C., Benítez Del Castillo, J.M., Geffen, D., Tauber, J., Foulks, G.N., Pepose, J.S., Sullivan, B.D.: Tear osmolarity in the diagnosis and management of dry eye disease. *Am.J. Ophthalmol.* **151**(5), 792–7981 (2011)

- [12] Li, L., Braun, R.J., Henshaw, W.D., King-Smith, P.E.: Computed flow and fluorescence over the ocular surface. *Math. Med. Biol.* **35**, 51–85 (2018)
- [13] Braun, R.J., Driscoll, T.A., Begley, C.G., King-Smith, P.E., Siddique, J.I.: On tear film breakup (TBU): Dynamics and imaging. *Math. Med. Biol.: A Journal of the IMA* **35**(2), 145–180 (2018)
- [14] Braun, R.J., King-Smith, P.E., Begley, C.G., Li, L., Gewecke, N.R.: Dynamics and function of the tear film in relation to the blink cycle. *Prog. Ret. Eye Res.* **45**, 132–164 (2015)
- [15] Holly, F.J.: Formation and rupture of the tear film. *Exp. Eye Res.* **15**(5), 515–525 (1973)
- [16] King-Smith, P.E., Fink, B.A., Hill, R.M., Koelling, K.W., Tiffany, J.M.: The thickness of the tear film. *Curr. Eye Res.* **29**(4-5), 357–368 (2004)
- [17] Mishima, S., Maurice, D.M.: The oily layer of the tear film and evaporation from the corneal surface. *Exp. Eye Res.* **1**, 39–45 (1961)
- [18] Gipson, I.K.: Distribution of mucins at the ocular surface. *Exp. Eye Res.* **78**(3), 379–388 (2004)
- [19] Dartt, D.A.: Neural regulation of lacrimal gland secretory processes: Relevance in dry eye diseases. *Prog. Ret. Eye Res.* **28**(3), 155–177 (2009)
- [20] Braun, R.J.: Dynamics of the Tear Film. *Annu. Rev. Fluid Mech.* **44**(1), 267–297 (2012)
- [21] Norn, M.S.: Micropunctate Fluorescein Vital Staining of the Cornea. *Acta Ophthalmol.* **48**(1), 108–118 (1970)
- [22] Cho, P., Brown, B., Chan, I., Conway, R., Yap, M.: Reliability of the tear break-up time technique of assessing tear stability and the locations of the tear break-up in Hong Kong Chinese. *Optom. Vis. Sci.* **69**(11), 879–885 (1992)
- [23] Dibajnia, P., Mohammadinia, M., Moghadasin, M., Amiri, M.A.: Tear Film Break-up Time in Bipolar Disorder. *Iranian J. Psych.* **7**(4), 191–193 (2012)
- [24] Sharma, A., Tiwari, S., Khanna, R., Tiffany, J.M.: Hydrodynamics of Meniscus-induced Thinning of the Tear Film. In: Sullivan, D.A., Dartt, D.A., Meneray, M.A. (eds.) *Advances in Experimental Medicine and Biology. Lacrimal Gland, Tear Film, and Dry Eye Syndromes 2*, vol. 438, pp. 425–431. Springer, Berlin (1998)
- [25] Wong, H., Fatt, I., Radke, C.J.: Deposition and thinning of the human tear film. *J. Colloid Interface Sci.* **184**(1), 44–51 (1996)

- [26] Miller, K.L., Polse, K.A., Radke, C.J.: Black line formation and the “perched” human tear film. *Curr. Eye Res.* **25**, 155–62 (2002)
- [27] Braun, R.J., Fitt, A.D.: Modeling the drainage of the precorneal tear film after a blink. *Math. Med. Biol.* **20**, 1–28 (2003)
- [28] Li, L., Braun, R.J.: A model for the human tear film with heating from within the eye. *Phys. Fluids* **24**(6), 062103 (2012)
- [29] Dursch, T.J., Li, W., Taraz, B., Lin, M.C., Radke, C.J.: Tear-film evaporation rate from simultaneous ocular-surface temperature and tear-breakup area. *Optom. Vis. Sci.* **95**, 5–12 (2018)
- [30] Peng, C.-C., Cerretani, C., Braun, R.J., Radke, C.J.: Evaporation-driven instability of the precorneal tear film. *Adv. Coll. Interface Sci.* **206**, 250–264 (2014)
- [31] Zhong, L., Braun, R.J., Begley, C.G., King-Smith, P.E.: Dynamics of Fluorescent Imaging for Rapid Tear Thinning. *Bull. Math. Biol.* **81**(1), 39–80 (2019)
- [32] Luke, R.A., Braun, R.J., Driscoll, T.A., Begley, C.G., Awisi-Gyau, D.: Parameter Estimation for Evaporation-Driven Tear Film Thinning. *Bull. Math. Biol.* **82**(6), 71 (2020)
- [33] Luke, R.A., Braun, R.J., Driscoll, T.A., Awisi-Gyau, D., Begley, C.G.: Parameter Estimation for Mixed-Mechanism Tear Film Thinning. *Bull. Math. Biol.* **83**(5), 56 (2021)
- [34] Luke, R.A., Braun, R.J., Driscoll, T.A., Sinopoli, D., Yawatkar, V., You, L., Phatak, A., Begley, C.G.: Fitting Simplified Models to Machine Learning-Identified Tear Film Breakup. *Invest. Ophthalmol. Vis. Sci.* **62**(8), 1315–1315 (2021)
- [35] Driscoll, T.A., Braun, R.J., Luke, R.A., Sinopoli, D., Phatak, A., Dorsch, J., Begley, C.G., Awisi-Gyau, D.: Fitting ODE models of tear film breakup. *Model. Artif. Intell. Ophthalmol.* **5**, 1–36 (2023)
- [36] Ji, H., Witelski, T.P.: Finite-time thin film rupture driven by modified evaporative loss. *Physica D: Nonlinear Phenomena* **342**, 1–15 (2017)
- [37] Ji, H., Witelski, T.P.: Steady states and dynamics of a thin-film-type equation with non-conserved mass. *Eur. J. Appl. Math.* **31**, 968–1001 (2020)
- [38] Shi, X., Rodríguez-Hakim, M., Shaqfeh, E.S.G., Fuller, G.G.: Instability and symmetry breaking in binary evaporating thin films over a solid spherical dome. *J. Fluid Mech.* **915**, 45 (2021)
- [39] Shi, X., Fuller, G.G., Shaqfeh, E.S.G.: Instability and symmetry breaking of

- surfactant films over an air bubble. *J. Fluid Mech.* **953**, 26 (2022)
- [40] Zhang, Y.L., Matar, O.K., , Craster, R.V.: Analysis of tear film rupture: Effect of non-newtonian rheology. *J. Colloid Interface Sci.* **262**, 130–148 (2003)
- [41] Zhang, Y.L., Matar, O.K., , Craster, R.V.: Rupture analysis of the corneal mucus layer of the tear film. *Mol. Simul.* **30**, 167–172 (2004)
- [42] Zhong, L., Ketelaar, CF., Braun, R.J., Begley, CG., King-Smith, PE.: Mathematical modelling of glob-driven tear film breakup. *Math. Med. Biol.* **36**(1), 55–91 (2018)
- [43] Dey, M., Vivek, A.S., Dixit, H.N., Richhariya, A., Feng, J.J.: A model of tear-film breakup with continuous mucin concentration and viscosity profiles. *J. Fluid Mech.* **858**, 352–376 (2019)
- [44] Dey, M., Vivek, A.S., Dixit, H.N., Richhariya, A., Feng, J.J.: A model of tear-film breakup with continuous mucin concentration and viscosity profiles—Corrigendum. *J. Fluid Mech.* **889**, 1 (2020)
- [45] Choudhury, A., Dey, M., Dixit, H.N., Feng, J.J.: Tear-film breakup: The role of membrane-associated mucin polymers. *Phys. Rev. E* **103**, 013018 (2021)
- [46] Madl, A.C., Fuller, G.G., Myung, D.: Modeling and restoring the tear film. *Curr. Ophthalmol. Rep.* **8**, 281–300 (2020)
- [47] Madl, A.C., Liu, C., Cirera-Salinas, D., Fuller, G.G., Myung, D.: A mucin-deficient ocular surface mimetic platform for interrogating drug effects on biolubrication, antiadhesion properties, and barrier functionality. *ACS Appl. Mater. Interfaces* **14**(16), 18016–18030 (2022)
- [48] King-Smith, P.E., Kimball, S.H., Nichols, J.J.: Tear film interferometry and corneal surface roughness. *Invest. Ophthalmol. Vis. Sci.* **55**(4), 2614–2618 (2014)
- [49] King-Smith, P.E., Hinel, E.A., Nichols, J.J.: Application of a novel interferometric method to investigate the relation between lipid layer thickness and tear film thinning. *Invest. Ophthalmol. Vis. Sci.* **51**(5), 2418–2423 (2010)
- [50] Wang, J., Fonn, D., Simpson, T.L., Jones, L.: Precorneal and Pre- and Postlens Tear Film Thickness Measured Indirectly with Optical Coherence Tomography. *Invest. Ophthalmol. Vis. Sci.* **44**(6), 2524 (2003)
- [51] Webber, W.R., Jones, D.P.: Continuous fluorophotometric method of measuring tear turnover rate in humans and analysis of factors affecting accuracy. *Med. Biol. Eng. Comput.* **24**(4), 386–392 (1986)
- [52] Benedetto, D.A., Clinch, T.E., Laibson, P.R.: In Vivo Observation of Tear Dynamics Using Fluorophotometry. *Archives of Ophthalmology* **102**(3), 410–412

(1984)

- [53] Begley, C.G., Simpson, T.L., Liu, H., Salvo, E., Wu, Z., Bradley, A., Situ, P.: Quantitative analysis of tear film fluorescence and discomfort during tear film instability and thinning. *Invest. Ophthalmol. Vis. Sci.* **54**(4), 2645–2653 (2013)
- [54] Himebaugh, N.L., Nam, J., Bradley, A., Liu, H., Thibos, L.N., Begley, C.G.: Scale and spatial distribution of aberrations associated with tear breakup. *Optom. Vis. Sci.* **89**(11), 1590–1600 (2012)
- [55] Awisi-Gyau, D., Begley, C.G., Situ, P., Simpson, T.L.: Changes in Corneal Detection Thresholds After Repeated Tear Film Instability. *Invest. Ophthalmol. Vis. Sci.* **60**(13), 4234–4240 (2019)
- [56] Nichols, J.J., Mitchell, G.L., King-Smith, P.E.: Thinning Rate of the Precorneal and Prelens Tear Films. *Invest. Ophthalmol. Vis. Sci.* **46**(7), 2353 (2005)
- [57] Stapf, M.R., Braun, R.J., King-Smith, P.E.: Duplex tear film evaporation analysis. *Bull. Math. Biol.* **79**(12), 2814–2846 (2017)
- [58] Zhornitskaya, L., Bertozzi, A.L.: Positivity-Preserving Numerical Schemes for Lubrication-Type Equations. *SIAM J. Num. Anal.* **37**(2), 523–555 (1999)
- [59] Oron, A., Bankoff, S.G.: Dynamics of a condensing liquid film under conjoining/disjoining pressures. *Phys. Fluids* **13**(5), 1107–1117 (2001)
- [60] Schwartz, L.W., Roy, R.V., Eley, R.R., Petrash, S.: Dewetting Patterns in a Drying Liquid Film. *J. Coll. Interface Sci.* **234**(2), 363–374 (2001)
- [61] Lee, Y.C., Thompson, H.M., Gaskell, P.H.: An efficient adaptive multigrid algorithm for predicting thin film flow on surfaces containing localised topographic features. *Comput. Fluids* **36**(5), 838–855 (2007)
- [62] Heryudono, A., Braun, R.J., Driscoll, T.A., Maki, K.L., Cook, L.P., King-Smith, P.E.: Single-equation models for the tear film in a blink cycle: Realistic lid motion. *Math. Med. Biol.* **24**(4), 347–377 (2007)
- [63] Grün, G., Rumpf, M.: Nonnegativity preserving convergent schemes for the thin film equation. *Numerische Mathematik* **87**(1), 113–152 (2000)
- [64] Maki, K.L., Braun, R.J., Ucciferro, P., Henshaw, W.D., King-Smith, P.E.: Tear film dynamics on an eye-shaped domain. Part 2. Flux boundary conditions. *J. Fluid Mech.* **647**, 361–390 (2010)
- [65] Li, L., Braun, R.J., Maki, K.L., Henshaw, W.D., King-Smith, P.E.: Tear film dynamics with evaporation, wetting, and time-dependent flux boundary condition on an eye-shaped domain. *Phys. Fluids* **26**(5), 052101 (2014)

- [66] Li, L., Braun, R.J., Driscoll, T.A., Henshaw, W.D., Banks, J.W., King-Smith, P.E.: Computed tear film and osmolarity dynamics on an eye-shaped domain. *Math. Med. Biol.* **33**(2), 123–157 (2016)
- [67] Gräßle, C., Hinze, M.: POD Reduced Order Modeling for Evolution Equations Utilizing Arbitrary Finite Element Discretizations. arXiv (2020)
- [68] Weiss, J.: A Tutorial on the Proper Orthogonal Decomposition (2019) <https://doi.org/10.14279/DEPOSITONCE-8512>
- [69] Berger, R.E., Corrsin, S.: A surface tension gradient mechanism for driving the pre-corneal tear film after a blink. *J. Biomech.* **7**, 225–38 (1974)
- [70] Braun, R.J., Usha, R., McFadden, G.B., Driscoll, T.A., Cook, L.P., King-Smith, P.E.: Thin film dynamics on a prolate spheroid with application to the cornea. *J. Eng. Math.* **73**, 121–138 (2012)
- [71] Allouche, M., Abderrahmane, H.A., Djouadi, S.M., Mansouri, K.: Influence of curvature on tear film dynamics. *Eur. J. Mech. B Fluids* **66**, 81–91 (2017)
- [72] Oron, A., Davis, S.H., Bankoff, S.G.: Long-scale evolution of thin liquid films. *Rev. Mod. Phys.* **69**, 931–980 (1997)
- [73] Craster, R.V., Matar, O.K.: Dynamics and stability of thin liquid films. *Rev. Mod. Phys.* **81**, 1131–1198 (2009)
- [74] Jensen, O.E., Grotberg, J.B.: The spreading of heat or soluble surfactant along a thin liquid film. *Phys. Fluids A* **75**, 58–68 (1993)
- [75] Tiffany, J.M.: The viscosity of human tears. *Internat. Ophthalmol.* **15**(6), 371–376 (1991)
- [76] Nagyová, B., Tiffany, J.M.: Components responsible for the surface tension of human tears. *Current Eye Research* **19**(1), 4–11 (1999)
- [77] Casalini, T., Salvalaglio, M., Perale, G., Masi, M., Cavallotti, C.: Diffusion and aggregation of sodium fluorescein in aqueous solutions. *J. Phys. Chem.. B* **115**(44), 12896–12904 (2011)
- [78] Riquelme, R., Lira, I., Pérez-López, C., Rayas, J.A., Rodríguez-Vera, R.: Interferometric measurement of a diffusion coefficient: Comparison of two methods and uncertainty analysis. *J. Phys. D: Appl. Phys.* **40**(9), 2769–2776 (2007)
- [79] Mota, M.C., Carvalho, P., Ramalho, J., Leite, E.: Spectrophotometric analysis of sodium fluorescein aqueous solutions. Determination of molar absorption coefficient. *Internat. Ophthalmol.* **15**(5), 321–326 (1991)
- [80] King-Smith, P.E., Reuter, K.S., Braun, R.J., Nichols, J.J., Nichols, K.K.: Tear

- film breakup and structure studied by simultaneous video recording of fluorescence and tear film lipid layer, TFLL, images. *Invest. Ophthalmol. Vis. Sci.* **54**, 4900–4909 (2013)
- [81] Braun, R.J., Gewecke, N.R., Begley, C.G., King-Smith, P.E., Siddique, J.I.: A Model for Tear Film Thinning With Osmolarity and Fluorescein. *Invest. Ophthalmol. Vis. Sci.* **55**(2), 1133–1142 (2014)
- [82] Trefethen, L.N.: *Spectral Methods in Matlab. Software, Environments, Tools.* SIAM, Philadelphia (2000)
- [83] Rackauckas, C., Nie, Q.: *Differentialequations.jl—a performant and feature-rich ecosystem for solving differential equations in julia.* *Journal of Open Research Software* **5**(1), 15 (2017)
- [84] Shampine, L.F., Reichelt, M.W.: *The matlab ode suite.* *SIAM journal on scientific computing* **18**(1), 1–22 (1997)
- [85] Liu, H., Begley, C.G., Chen, M., Bradley, A., Bonanno, J., McNamara, N.A., Nelson, J.D., Simpson, T.: A link between tear instability and hyperosmolarity in dry eye. *Invest. Ophthalmol. Vis. Sci.* **50**(8), 3671–3679 (2009)
- [86] Li, W., Graham, A.D., Selvin, S., Lin, M.C.: Ocular surface cooling corresponds to tear film thinning and breakup. *Optom. Vis. Sci.* **92**, 248–256 (2015)